inorganics

MDPI

Article

Gold(III) Pyridine-Benzimidazole Complexes as Aquaglyceroporin Inhibitors and Antiproliferative Agents

Brech Aikman [1,†], Margot N. Wenzel [1,†], Andreia F. Mósca [2,†], Andreia de Almeida [1,3], Wim T. Klooster [4], Simon J. Coles [4], Graça Soveral [2,*] and Angela Casini [1,*]

1 School of Chemistry, Cardiff University, Main Building, Park Place, Cardiff CF10 3AT, UK; AikmanB@cardiff.ac.uk (B.A.); WenzelM3@cardiff.ac.uk (M.N.W.); dealmeidaa@cardiff.ac.uk (A.d.A.)
2 Research Institute for Medicines (iMed.ULisboa), Faculty of Pharmacy, Universidade de Lisboa, 1649-003 Lisboa, Portugal; andreiafbm@ff.ulisboa.pt
3 Tumour MicroEnvironment Group, Division of Cancer and Genetics, School of Medicine, Cardiff University, Tenovus Building, Cardiff CF14 4XN, UK
4 School of Chemistry, University of Southampton, Southampton SO17 1BJ, UK; W.T.Klooster@soton.ac.uk (W.T.K.); S.J.Coles@soton.ac.uk (S.J.C.)
* Correspondence: gsoveral@ff.ulisboa.pt (G.S.); casinia@cardiff.ac.uk (A.C.); Tel.: +351-217946461 (G.S.); +44-29-2087-6364 (A.C.)
† These authors contributed equally to this work.

Received: 11 October 2018; Accepted: 15 November 2018; Published: 20 November 2018

Abstract: Gold compounds have been proven to be novel and versatile tools for biological applications, including as anticancer agents. Recently, we explored the potential of Au(III) complexes with bi-dentate N-donor ligands as inhibitors of the membrane water and glycerol channels aquaporins (AQPs), involved in different physiological and pathophysiological pathways. Here, eight new Au(III) complexes featuring a pyridine-benzimidazole scaffold have been synthesized and characterized via different methods. The stability of all the compounds in aqueous solution and their reactivity with glutathione have been investigated by UV–visible spectroscopy. The Au(III) compounds, tested for their AQPs inhibition properties in human Red Blood Cells (hRBC), are potent and selective inhibitors of AQP3. Furthermore, the compounds' antiproliferative effects have been studied in a small panel of human cancer cells expressing AQP3. The complexes show only very moderate anticancer effects in vitro and are mostly active against the melanoma A375 cells, with marked expression of AQP3 at the level of the nuclear membrane. In general, the AQP3 inhibition properties of these complexes hold promises to develop them as chemical probes to study the function of this protein isoform in biological systems.

Keywords: Gold(III) complexes; pyridine benzimidazole; aquaporins; cancer; stopped-flow spectroscopy; antiproliferative activity

1. Introduction

The severe side effects associated with chemotherapy necessitate the development of improved anticancer therapies. Specifically, the discovery of compounds that can disrupt cancerous cellular machinery by novel mechanisms of action is nowadays the focus of intense research. For example, metal-based compounds acting via the interaction with proteins and secondary DNA structures, as well as by alteration of the intracellular redox balance, have become prominent experimental therapeutic agents. Among them, gold complexes have attracted attention in the last years and numerous families of Au(I) and Au(III) compounds have been synthesized and studied for their anticancer properties

in vitro and in vivo [1,2]. Overall, the investigation of the cytotoxic activity and related mode of action of cytotoxic gold-based complexes has enabled the identification of their preferential "protein targets", as it is increasingly evident that DNA is not the unique or major target for such compounds [3]. In this context, coordination cytotoxic Au(III) compounds have been identified as selective inhibitors of the membrane water channels aquaporins (AQPs) [1,4].

Among the 13 mammalian AQPs described so far, three sub-groups can be recognized based on permeability features: *orthodox aquaporins* (AQP0, AQP1, AQP2, AQP4, AQP5, AQP6 and AQP8), which are primarily water selective and facilitate water movement across cell membranes in response to osmotic gradients [5]; *aquaglyceroporins* (AQP3, AQP7, AQP9 and AQP10), facilitating the permeation of small uncharged solutes such as glycerol [6]; and *unorthodox* aquaporins (AQP11, AQP12), found in intracellular membranes and with reported permeability to water and glycerol [7–9]. Specifically, the aquaglyceroporins regulate the glycerol content in the epidermis, fat and other tissues and appear to be involved in skin hydration, cell proliferation, fat metabolism, and carcinogenesis. Several studies showed that AQPs are closely associated with cancer proliferation and invasion, and are expressed in at least 20 human cancers [10]. Moreover, AQPs expression is related to tumour types, grades, proliferation, migration and angiogenesis, rendering these transport proteins attractive as both diagnostic and therapeutic targets in cancer [10]. To validate the various roles of AQPs in health and disease, and to develop AQP-targeted therapies, the use of selective inhibitors in addition to genetic approaches, holds great promise. However, so far, no reported organic small-molecule AQPs inhibitor possesses sufficient isoform selectivity to be a good candidate for clinical development [11].

A few years ago, we reported on the potent and selective inhibition of human AQP3 by a series of Au(III) complexes with bidentate N^N ligands [12,13], which could potently and selectively inhibit glycerol permeation through hAQP3 in human red blood cells (hRBC). The most effective inhibitor of the series, Auphen ([Au(phen)Cl_2]Cl, phen = 1,10-phenanthroline) had an IC_{50} of 0.8 ± 0.08 μM [12]. In a further study, Auphen's capacity of inhibiting cell proliferation was examined in various cell lines, including cancerous ones, with different levels of AQP3 expression, and showed a direct correlation between AQP3 expression levels and the inhibition of cell growth by the Au(III) compound [14]. AQP3 inhibition was also demonstrated in the cell lines where proliferation was mostly affected by treatment with the gold complex [14]. Structure–activity relationships to optimize the design of AQP3 inhibitors were then established investigating other Au(III) compounds with different N^N ligand scaffolds [13].

Pursuing the design of more potent and selective AQP3 inhibitors, we have recently observed that the cationic complex [Au(pbzMe)Cl_2]PF_6 (**C1**, pbzMe = 1-methyl-2-(pyridin-2-yl)-benzimidazole) is even more efficient than Auphen in inhibiting glycerol permeation via AQP3 [1], and ca. three orders of magnitude more effective than the neutral related complex [Au(pbzH)Cl_2] (**C10**, pbzH = 2-(pyridin-2-yl)-benzimidazole) [15]. Combined molecular dynamics (MD) and density functional theory (DFT) studies were able to show that **C1**, upon binding to Cys40 in AQP3, is able to induce protein conformational changes, leading to the shrinkage of the channel, and thus, preventing glycerol and water permeation [15].

Following these promising results, we have synthesized a new series of Au(III) complexes based on the 2-(2-pyridyl)benzimidazole (pbzH) N-donor ligand, which is also known to inhibit hepatic enzymes, [16] and exhibits anticancer activities *per se* [17]. In general, metal complexes based on 2-(2′-pyridyl)benzimidazole scaffolds have attracted attention in various established and potential application areas, including medicinal inorganic chemistry [18–20]. Thus, we report here on the synthesis and characterization of eight new cationic Au(III) derivatives with functionalization at the non-coordinated benzimidazole nitrogen. In addition, two neutral complexes featuring extended aromatic scaffolds (namely pyrene and anthracene), endowed with luminescence properties, have been obtained. The compounds have been tested for their AQPs inhibition properties in human Red Blood Cells (hRBC) using a stopped-flow method, and their effects compared to **C1** [Au(pbzMe)Cl_2]PF_6 and

C10 [Au(pbzH)Cl_2]. Furthermore, the compounds' antiproliferative effects have been studied in a small panel of human cancer cells with different levels of AQP3 expression.

2. Results

2.1. Synthesis and Characterization of Au(III) Complexes

The library of functionalised pyridylbenzimidazole ligands **L1**–**L9** has been obtained by nucleophilic substitution on the non-coordinated nitrogen atom of the commercially available pyridylbenzimidazole by reaction with a halogenated substituent (R–X) in the presence of a base (Scheme S1, Supplementary Materials) [21]. Several types of functional groups have been envisaged to study the influence of both the steric hindrance and the electronic effect on the biological properties of the final gold complexes. In parallel, two additional ligands (**L11**–**L12**) featuring luminescent properties [22] have also been synthesized with the idea to monitor their fate in cancer cells by fluorescence microscopy (Scheme S1, supplementary materials). The use of ligands **L1**–**L9**, which possess a functionalised amine, gives rise to Au(III) cationic complexes (corresponding **C1**–**C9**) by reaction between an equimolar amount of **L1**–**L9** and $NaAuCl_4$, in the presence of an excess of KPF_6 (Scheme 1, top). The pure cationic gold complexes can then easily be isolated following precipitation, washing and filtration. On the other hand, reaction between ligands **L10**–**L12** and $NaAuCl_4$ in the presence of a base leads to the formation of the neutral complexes **C10**–**C12** (Scheme 1, bottom) [15]. The identity and the purity of the complexes **C1**–**C12** was confirmed by NMR, IR and UV–Visible spectroscopies, as well as by mass spectrometry and in some cases by elemental analysis (See Experimental and Supplementary Materials for details, Figures S1–S24). The obtained results confirmed the purity of the compounds, which were all obtained in good yields. While all ligands were found to be soluble in most organic solvents, and thus, their NMR analysis was performed in $CDCl_3$, the complexes were insoluble in most cases, except in rare examples in acetone or acetonitrile. To ensure a similar analysis for all complexes, their NMR spectra were recorded in DMSO-d_6. The ^{1}H NMR spectra of the ligands were easily attributable and the most downfield shifted signals corresponded to the benzimidazole ring. In most cases, the signals of the protons of the pyridyl were found overlapping each other, in addition to the signals of the phenyl rings for the R substituents in the case of **L4**–**L9**. The ^{1}H NMR spectra of the complexes were similar to those of the corresponding ligands in terms of number of resonance signals; however, some signals (H_a, H_c and H_h, see Scheme 2 for the numbering scheme) were clearly more affected by the presence of the Au(III)Cl_2 fragment [$\Delta\delta$ ($\delta_{coord} - \delta_{free}$) of 0.24 and 0.47 ppm]. The NMR analysis of both the ligands **L11**–**L12** and their corresponding complexes **C11** and **C12** was very challenging due to the electronic similarity and thus proximity on the spectra. However, the number and nature of the signals were compatible with the structures, and further analytical methods allowed us to confirm the purity of the compounds (ESI-MS, UV–Visible spectroscopy and IR). IR analysis of the complexes showed in all cases the presence of C=C bending, C–H stretching and C–N stretching bands, and confirmed the presence of specific chemical groups on the main scaffold: alkyl chains in the case of **C1**–**C3**, ester group in the case of **C5** and C–F bonds for **C6**–**C9**.

Crystals suitable for X-ray diffraction were obtained for complex **C6** by slow diffusion of pentane in a concentrated solution of the complex in a mixture of acetonitrile and dichloromethane at room temperature (see Supplementary Materials for details). The structure confirmed a bidentate coordination mode of the ligand **L6** onto the gold centre via the nitrogen of the pyridine and the benzimidazole rings, giving rise to square planar complexes. The 4-trifluoromethylbenzyl functional group added on the benzimidazole moiety always points out of the plane, as already described with similar ligands and copper complexes [18]. It is worth mentioning that the slow process of crystallisation (10–15 days) may favour the partial decomposition of the complexes, specifically the de-coordination of the gold centre and the exchange of counter anions. In fact, the structure of **C6** revealed the presence of $AuCl_4$ counterions in the lattice (see Supplementary Materials).

Furthermore, we attempted to crystallize compound **C7** in the same conditions, but the resulting X-ray structure confirmed the de-coordination of the gold centre from one of the nitrogens of the pyridine ligand, thus leading to a neutral gold complex with three coordinated chlorido ligands (see supplementary materials).

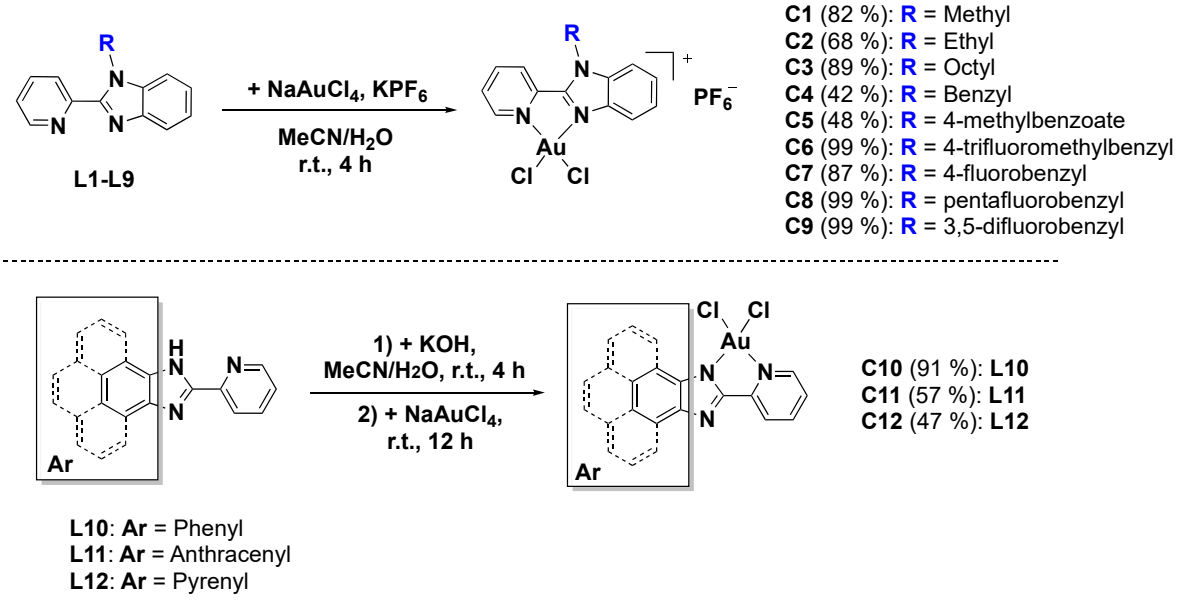

Scheme 1. Synthetic pathways to the series of cationic (top) and neutral (bottom) Au(III) complexes **C1**–**C9** and **C10**–**C12**, respectively.

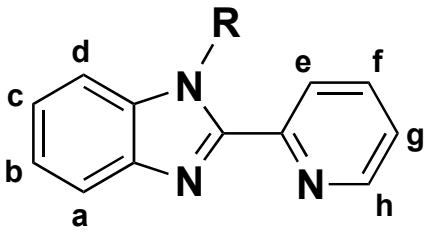

Scheme 2. ^{1}H labelling in the selected ligand scaffold.

The complexes **C1**–**C12** and their corresponding ligands **L1**–**L12** have also been investigated for their photophysical properties (see Figures S25–S48). Both ligands **L1**–**L10** and complexes **C1**–**C9** exhibit a strong absorption band centred around 310–315 nm which can be attributed to $\pi \rightarrow \pi^*$ transitions and/or ligand-to-metal charge transfers (LMCT) in the case of the Au(III) complexes. The absorption spectra of ligands **L11**–**L12** and corresponding complexes **C11**–**C12**, with the extended conjugated systems, show several bands attributed to the same transitions between 330 and 390 nm. Ligands **L1**–**L10** and complexes **C1**–**C9** all have single fluorescence emission bands centred around 375–380 nm, representing a Stokes shift of about 65 nm. Complexes **C11**–**C12** and their corresponding ligands possess extended aromatic and conjugated systems; thus, a shift in the emission bands is observed: ligand **L11** and complex **C11** emit at 415 nm whereas **L12** and **C12** exhibit an emission band around 450 nm (Figures S45–S48). The quantum yield of fluorescence (Φ_F) has also been assessed for all the reported compounds (see Figures S25–S48). While the ligands with the alkane substituents (**L1**–**L3**) have relatively high quantum yields (50–60%), the ligands with the functionalised benzyl groups (**L4**–**L9**) have decreased quantum yields between 27 and 42%. The ligands with the extended aromatic systems **L11** and **L12** have quantum yields of 74 and 61%, respectively (Figures S45 and S47). In general, upon coordination of the ligands to the gold(III) ion, almost all quantum yields of luminescence are decreased due to the "heavy metal effect", with the exception of complex **C12** (Φ_F = 71%).

2.2. UV–Visible Stability Studies

The stability of the gold complexes was investigated using UV–Visible spectroscopy before further biological testing. Thus, the absorbance of the compounds' solutions in PBS buffer (pH 7.4) was measured between 300 and 800 nm at regular time intervals during 24 h at room temperature, allowing the monitoring of possible compound's transformations such as hydrolysis, reduction and/or precipitation. In parallel, as Au(III) complexes tend to be reduced in physiological conditions to Au(I) and even Au(0), the reactivity of the compounds with the intracellular reducing agent glutathione (GSH) was monitored in the same conditions.

All the Au(III) compounds exhibit intense transitions in the 300–400 nm range, characteristic of the Au(III) chromophore, that may be straightforwardly assigned as LMCT bands. Complexes **C1**, **C2**, **C5**, **C6** and **C9** were found to be mostly stable over the first 6 h in PBS buffer (pH 7.4) with no significant change in the UV–Visible spectra (Figures S49, S50, S53, S54 and S57). The observed small spectral changes developing with time might be related to the occurrence of partial hydrolysis processes. Instead, the spectra of complexes **C3**, **C4**, **C7**, **C8** and **C10** were found to undergo major changes over the first few hours (Figures S51–S52, S55–S56 and S58), leading to the disappearance of the classical LMCT bands, suggesting disruption of the Au(III) complex. Complexes **C11**–**C12** were moderately stable in solution (Figures S59 and S60) featuring hypocromic shifts in their spectra over the first 6 h of incubation. In the presence of GSH, all the compounds immediately reacted to form adducts leading to the loss of the N-donor ligands from the gold centre, as demonstrated by the disappearance of the LMCT bands (Figures S49–S58). Only compounds **C11** and **C12** were scarcely reactive and maintained their spectral features over time after the addition of GSH (Figures S59 and S60).

2.3. Inhibition of Aquaporins

Based on the previosuly discussed stability studies, only the most stable gold complexes were tested for their AQP1 and AQP3 inhibition properties in hRBC by stopped-flow spectroscopy, according to previously reported procedures [12]. A representative IC_{50} curve for the inhibition of glycerol permeation via AQP3 by two gold compounds is reported in Figure 1. The obtained results are summarized in Table 1 and show that all the new cationic complexes **C2**, **C4**, **C5**, **C6**, **C9** and **C11** are able to selectively inhibit glycerol permeation via AQP3, with IC_{50} values in the sub-micromolar level, comparable to **C1** and Auphen. The antiproliferative activities of the corresponding ligands are presented in the supplementary (Table S1). The most effective compound was **C6**. In line with previous results, the neutral compound **C10** was ca. one order of magnitude less effective as an AQP3 inhibtior [15]. Of note, all the compounds were inactive as inhibitors of the orthodox water channel AQP1 in the same cellular model (data not shown).

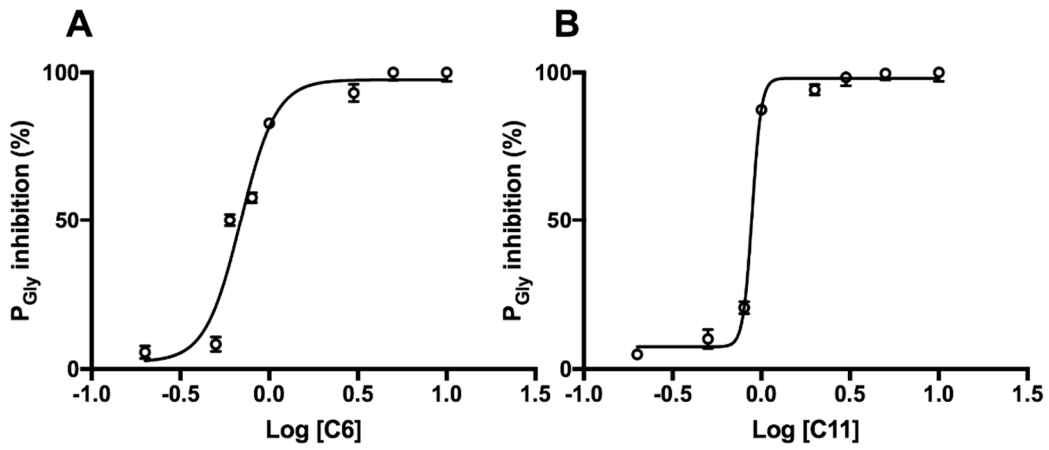

Figure 1. Representative IC_{50} curve for the inhibition of glycerol permeation via AQP3 by the Au(III) complexes **C6** (**A**) and **C11** (**B**) in hRBC after 30 min incubation.

Table 1. AQP3 inhibitory effects (IC_{50} values) measured in hRBC after 30 min incubation; and antiproliferative activities (EC_{50} values) of Au(III) compounds in human SKOV-3, A375, MCF-7, and A549 cells after 72 h incubation, measured by the MTT assay.

Compound	AQP3 Inhibition	EC_{50} [μM] [1]			
	IC_{50} [μM] [1]	SKOV-3	A375	MCF7	A549
Auphen	0.80 ± 0.08	7.00 ± 2.00	1.7 ± 0.3	3.00 ± 0.05	1.07 ± 0.09
C1	1.018 ± 0.137	>80	>80	>80	>80
C2	0.881 ± 0.015	>80	>80	>80	>80
C3	1.825 ± 0.017 (*n* = 2)	41 ± 13	23 ± 1	40 ± 4	57 ± 2
C4	0.85 ± 0.21	56 ± 12	69 ± 3	63 ± 1	81 ± 9
C5	0.80 ± 0.10	>50	>50	25 (*n* = 1)	>50)
C6	0.69 ± 0.06	>50	34 (*n* = 1)	38 (*n* = 1)	47 (*n* = 2)
C7	n.d.	n.d.	n.d.	n.d.	n.d.
C8	n.d.	n.d.	n.d.	n.d.	n.d.
C9	0.72 ± 0.05	>50	>50	>50	>50
C10	>50	17 ± 7	5 ± 2	12 ± 1	>50
C11	0.82 ± 0.13 (*n* = 2)	33 ± 5	12 ± 2	29 ± 8	>50
C12	n.d.	41 ±13	13 ± 2	17 ± 3	45 ± 3

[1] Values represented as mean (±SEM) of at least three independent experiments (*n*), unless otherwise stated. n.d. = non determined.

2.4. Expression of AQP3 in Cancer Cells and Antiproliferative Activities

Afterward, the compounds—with the exception of the highly unstable **C7** and **C8**—were evaluated for their antiproliferative activities against a panel of human cancer cells in vitro. The cells were selected and studied for their level of expression of human AQP3. Information on the expression of AQP3 in cancer lines is limited and most of the data currently available refers to mRNA expression levels [23]. Specifically, cells were studied for the expression levels of human AQP3 by flow cytometry (Figure S61) and their AQP3 cellular distribution by immunocytofluorescence, respectively (Figure 1). As expected from the literature and mRNA levels [23], the breast cancer cell line MCF-7 highly express AQP3. Ovarian cancer cells SKOV-3 also showed marked AQP3 expression, followed by the lung cancer cells A549 and the skin malignant melanoma cells A375. Regarding cellular localization, in the case of the melanoma cells A375, AQP3 was found to be also localized in the nuclear membrane (Figure 2) as evidenced by fluorescence microscopy.

The antiproliferative activities of the complexes are summarized in Table 1. Overall, the compounds show very moderate anticancer effects in all cell lines, with compounds **C1** and **C2** being the least toxic (EC_{50} > 80 μM). Compounds **C3** and **C4** were moderately cytotoxic, but their scarce stability in the aqueous environment may affect their antiproliferative effects. Compounds **C10**–**C12** were the most effective in the series, particularly against the melanoma A375 cells. It is worth mentioning that these three compounds are the only neutral ones, and may display different uptake and accumulation in cancer cells with respect to the cationic derivatives. Of note, the ligands **L1**–**L12** generally showed reduced antiproliferative effects with respect to the corresponding gold complexes (Table S1).

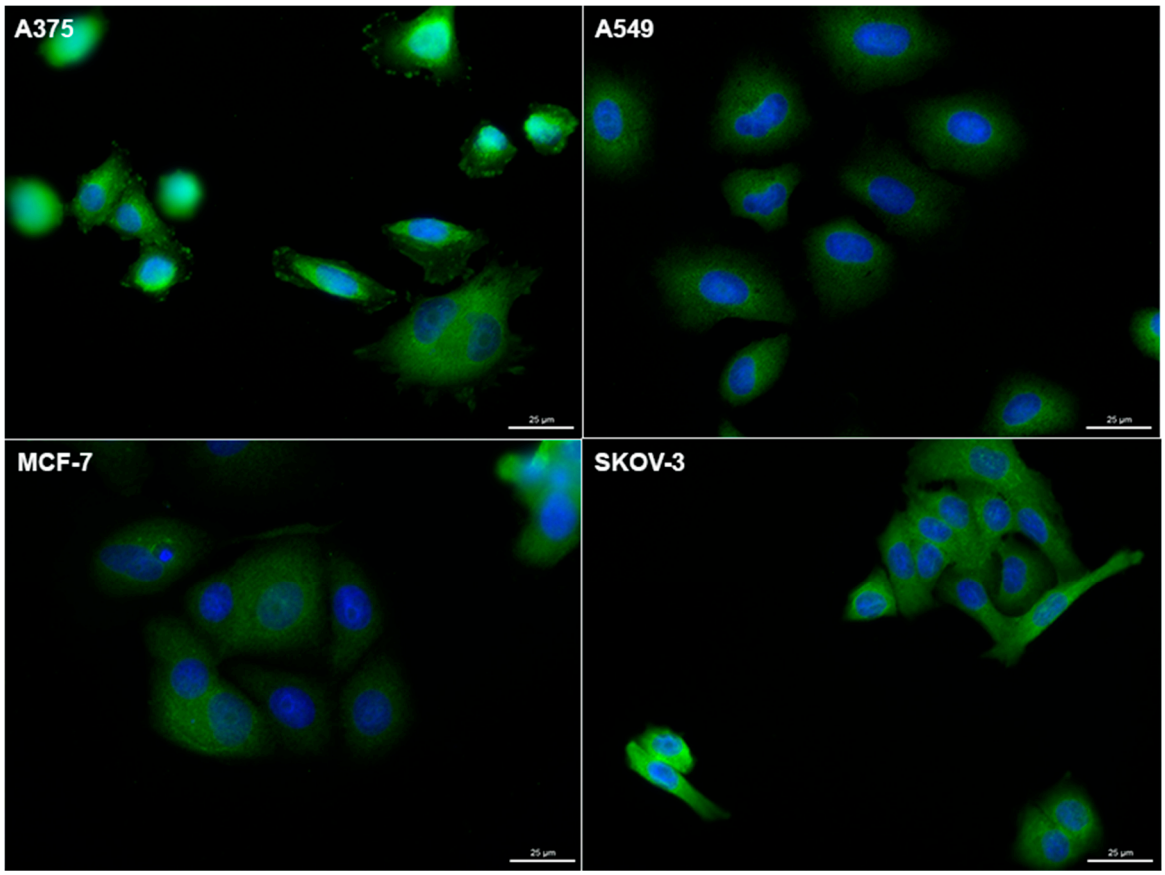

Figure 2. Human AQP3 expression and localization in human cancer cells by immunocytofluorescence. Human AQP3 expression (green) in A549, A375, SKOV-3 and MCF-7 cancer cells, with nuclei stained with DAPI (blue). Scale bars represent 25 μm.

3. Materials and Methods

3.1. General Information

All reagents and solvents used have been obtained from Haereus (Hanau, Germany), Sigma Aldrich (St. Louis, MO, United States), Fluorochem (Old Glossop, UK), Alfa Aesar (Ward Hill, MA, USA) or Acros (Loughborough, UK) and were used as received unless specified. The identity and purity (≥95%) of the complexes were unambiguously established using high-resolution mass spectrometry and multinuclear NMR spectroscopy. ^{1}H, ^{13}C and ^{19}F NMR spectra were recorded on a Bruker Avance II300, II400 or II500 spectrometers (Bruker, Coventry, UK) at room temperature (r.t.) and referenced internally to residual solvent peaks [24]. The coupling constants are reported in Hertz. HR-ESI-MS spectra were obtained in acetonitrile/methanol on a Thermo Finnigan LCQ DecaXPPlus quadrupole ion-trap instrument (Thermo Fisher Scientific, Paisley, UK) operated in positive ion mode over a mass range of m/z 150–2000. IR spectra were measured on a Shimadzu IRAffinity-1S FT-IR (ATR) (Shimadzu, Milton Keynes, UK). Ligand functionalization reactions were monitored by thin-layer chromatography (Merck 60 F254 silica gel). Column chromatography was carried out manually using silica gel (Fluorochem; 40–63 μm, 60 Å) or on a Biotage Isolera automated flash purification system (ZIP cartridge, 5–10 g). The absorption and emission spectra of the ligands and corresponding complexes were recorded on Cary 5000 or 60 UV–Visible NIR (Agilent, Wokingham, UK), Cary Eclipse Fluorescence spectrophotometers (Agilent).

3.2. Compounds Synthesis

3.2.1. General Procedure for the Synthesis of Ligands **L1**–**L9**

Pyridylbenzimidazole ligand **L10** is commercially available. Functionalised pyridylbenzimidazole derivatives **L1** [21], **L4** [25], **L7** [22], **L8** [22], **L9** [22], **L11** [25], and **L12** [18] have been synthetized following protocols reported in the literature. Ligands **L2** and **L3** have been obtained adapting protocols used to produce **L1** and **L4**, and have also been already reported in the literature [26]. The purity of the compounds was confirmed by elemental analysis, and all of them showed purity greater than 98%. Compounds **L5** and **L6** have been obtained using the following general protocol: A solution of 1 eq. of pyridylbenzimidazole (488 mg, 2.50 mmol) and 1.5 eq. of K_2CO_3 (518 mg, 3.75 mmol) in 5 mL of DMF was stirred at room temperature for 30 min. Then, 1.2 eq. (3.00 mmol) of methyl-4-(bromomethyl)benzoate (in the case of **L5**; 687 mg) or 4-(trifluoromethyl)benzyl bromide (in the case of **L6**; 717 mg) were added to the mixture and left to stir at room temperature for approximately 4 h (the reaction was followed by TLC using a 1:1 ethyl acetate/hexane eluent system). The solution was then concentrated and water was added. The product was extracted several times by ethyl acetate. Organic layers were combined, washed with water and dried over $MgSO_4$. After filtration and evaporation of the solvent, the crude products **L5** and **L6** were obtained and purified by column chromatography either manually using a 1:1 mixture of ethyl acetate and hexane or on an automated flash purification system using a gradient of ethyl acetate in hexane.

L5. White powder, 83% isolated yield (712 mg, 2.07 mmol). R_f (1:1 AcOEt/hexane) ≈ 0.6. NMR ^{1}H ($CDCl_3$): 8.56 (ddd, J = 7.9, 4.0 and 2.7 Hz, 1H, H_a), 8.44 (dt, J = 8.0 and 1.0 Hz, 1H, H_d), 7.92–7.87 (m, 3H, 2xCH–Ph + H_e), 7.81 (td, J = 8.0 and 1.8 Hz, 1H, H_c), 7.33–7.25 (m, 5H, H_h + H_b + H_f + H_g + H_e), 7.20 (d, J = 8.5 Hz, 2H, 2xCH–Ph), 6.14 (s, 2H, CH_2), 3.77 (s, 3H, CH_3). NMR ^{13}C{^{1}H} ($CDCl_3$): 166.8 (CO_2Me), 150.4 (C^{IV}), 149.9 (C^{IV}), 148.7 (C_a), 142.8 (C^{IV}), 142.8 (C^{IV}), 137.0 (C_c), 136.8 (C^{IV}), 130.0 (2xCH–Ph), 129.3 (C^{IV}), 126.7 (2xCH–Ph), 124.7 (C_d), 124.0, 123.9, 123.0 (C_b, C_f, C_g), 120.3 (C_e), 110.5 (C_h), 52.2 (CH_3), 48.9 (CH_2). ESI-TOF-MS (positive mode) for $C_{21}H_{18}N_3O_2$ ([M + H]$^+$): calc. 344.1399, exp. 344.1404 (err. 1.5 ppm). UV–Vis (DMSO): λ_{max} (nm) (ε, $cm^{-1}{\cdot}mol^{-1}{\cdot}dm^3$) 313 (14,123). IR (ATR): ν (cm^{-1}) 1709 ($\nu_{C–H\ bending}$), 1428 ($\nu_{C–H\ stretching}$), 1276 ($\nu_{C–O\ stretching}$), 1110 ($\nu_{C–N\ stretching}$), 845 ($\nu_{C=C\ bending}$). Anal. Calcd for $C_{21}H_{17}N_3O_2$ (343.39): C, 73.45; H, 4.99; N, 12.24. Found: C, 73.48; H, 4.97; N, 12.20.

L6. White powder, 88% isolated yield (774 mg, 2.19 mmol). R_f (1:1 AcOEt/hexane) ≈ 0.6. NMR ^{1}H ($CDCl_3$): 8.55 (m, 1H, H_a), 8.44 (d, J = 8.0 Hz, 1H, H_d), 7.84 (d, J = 7.8 Hz, 1H, H_e), 7.79 (td, J = 7.8 and 1.8 Hz, 1H, H_c), 7.46 (d, 2H, 2xCH–Ph), 7.47–7.22 (m, 6H, 2xCH–Ph + H_h + H_b + H_f + H_g), 6.20 (s, 2H, CH_2). NMR ^{13}C{^{1}H} ($CDCl_3$): 150.4 (C^{IV}), 149.8 (C^{IV}), 148.7 (C_a), 142.8 (C^{IV}), 141.7 (C^{IV}), 137.1 (C_c), 136.7 (C^{IV}), 129.7 (q, C^{IV}–CF_3, $^2J_{C–F}$ = 32.0 Hz), 126.8 (2xCH–Ph), 125.7 (q, 2xCH–C–CF_3, $^3J_{C–F}$ = 3.8 Hz), 124.7 (C_d), 124.2 (q, $C^{IV}F_3$, $^1J_{C–F}$ = 270 Hz), 124.1, 123.9, 123.2 (C_b, C_f, C_g), 120.4 (C_e), 110.4 (C_h), 48.7 (CH_2). NMR ^{19}F{^{1}H} ($CDCl_3$): −62.5 (s, CF_3). ESI-TOF-MS (positive mode) for $C_{20}H_{15}N_3F_3$ ([M + H]$^+$): calc. 354.1218, exp. 354.1225 (err. 2.0 ppm). UV–Vis (DMSO): λ_{max} (nm) (ε, $cm^{-1}{\cdot}mol^{-1}{\cdot}dm^3$) 313 (23,130). IR (ATR): ν (cm^{-1}) 1444 ($\nu_{C–H\ stretching}$), 1328, 1157 ($\nu_{C–F\ stretching}$), 1107 ($\nu_{C–N\ stretching}$), 833 ($\nu_{C=C\ bending}$). Anal. Calcd for $C_{20}H_{14}N_3F_3$ (353.11): C, 67.98; H, 3.99; N, 11.89. Found: C, 67.95; H, 3.93; N, 11.82.

3.2.2. General Procedure for the Synthesis of the Cationic Complexes **C1**–**C9**

Complex **C1** was previously reported by us [15], and the same procedure was used to obtain complexes **C2**–**C9**. Thus, to a solution of 1 eq. of pyridylbenzimidazole ligand **L1**–**L9** in acetonitrile (2.5 mL) was added an aqueous solution (15 mL) of 1 eq. of $NaAuCl_4$ and 3 eq. of KPF_6, and the resulting mixture was stirred 3 h at room temperature. The resulting yellow to orange precipitate was filtered, washed with water, ethanol and diethyl ether and dried under vacuum.

C2. Yield: 68% (480 mg, 0.76 mmol). NMR ^{1}H (DMSO-d_6): 8.93 (m, 1H, H_a), 8.29 (m, 1H, H_d), 8.21 (m, 1H, H_c), 8.05 (m, 1H, H_e), 7.89 (m, 1H, H_h), 7.76 (m, 1H, H_b), 7.61 (m, 2H, H_f + H_g), 4.87 (m, 2H, CH_2),

1.50 (s, 3H, CH_3). NMR ^{13}C{^{1}H} (DMSO-d_6): 150.2 (C_a), 146.8 (C^{IV}), 144.3 (C^{IV}), 138.3 (C_c), 133.3 (2xC^{IV}), 128.0 (C_g), 127.6 (C_f), 126.0 (C_d), 125.8 (C_b), 115.8 (C_h), 112.9 (C_e), 41.4 (CH_2), 14.9 (CH_3). ESI-TOF-MS (positive mode) for $C_{14}H_{13}N_3Cl_2Au$ ([M$^+$]): calc. 490.0152, exp. 490.0134 (err. −3.7 ppm). UV–Vis (DMSO): λ_{max} (nm) (ε, $cm^{-1}\cdot mol^{-1}\cdot dm^3$) 313 (21,654). IR (ATR): ν (cm^{-1}) 1475, 1457 ($\nu_{C–H\ stretching}$), 1036 ($\nu_{C–N\ stretching}$), 841, 749 ($\nu_{C=C\ bending}$).

C3. Yield: 89% (561 mg, 0.78 mmol). NMR ^{1}H (DMSO-d_6): 8.92 (m, 1H, H_a), 8.29–8.19 (m, 2H, H_d + H_c), 8.08 (m, 1H, H_e), 7.90 (m, 1H, H_h), 7.78 (m, 1H, H_b), 7.66–7.58 (m, 2H, H_f + H_g), 4.85 (m, 2H, CH_2), 1.85 (m, 2H, CH_2), 1.17 (m, 10H, CH_2), 0.82 (m, 3H, CH_3). NMR ^{13}C{^{1}H} (DMSO-d_6): 150.3 (C_a), 146.9 (C^{IV}), 143.9 (C^{IV}), 138.8 (C_c), 136.9 (C^{IV}), 133.6 (C^{IV}), 127.5 (C_g), 127.1 (C_f), 126.7 (C_d), 126.6 (C_b), 115.7 (C_h), 113.8 (C_e), 46.3 (CH_2), 31.6 (CH_2), 29.5 (CH_2), 28.9 (CH_2), 28.8 (CH_2), 26.2 (CH_2), 22.5 (CH_2), 14.4 (CH_3). ESI-TOF-MS (positive mode) for $C_{20}H_{25}N_3Cl_2Au$ ([M$^+$]): calc. 574.1091, exp. 574.1100 (err. 1.6 ppm). UV–Vis (DMSO): λ_{max} (nm) (ε, $cm^{-1}\cdot mol^{-1}\cdot dm^3$) 312 (16,006). IR (ATR): ν (cm^{-1}) 2927 ($\nu_{C–H\ stretching}$), 1488, 1474 ($\nu_{C–H\ stretching}$), 1039 ($\nu_{C–N\ stretching}$), 831, 746 ($\nu_{C=C\ bending}$).

C4. Yield: 99% (403 mg, 1.61 mmol). NMR ^{1}H (DMSO-d_6): 8.83 (m, 1H, H_a), 8.30 (m, 1H, H_d), 8.17 (m, 1H, H_c), 7.87 (m, 1H, H_e), 7.78 (m, 1H, H_h), 7.70 (m, 1H, H_b), 7.55–7.49 (m, 2H, H_f + H_g), 7.29–7.25 (m, 5H, 5xCH–Ph), 6.21 (s, 2H, CH_2). NMR ^{13}C{^{1}H} (DMSO-d_6): 149.9 (C_a), 147.2 (C^{IV}), 144.5 (C^{IV}), 138.1 (C_c), 135.5 (C^{IV}), 133.7 (C^{IV}), 128.6 (CH–Ph), 127.7 (CH–Ph), 126.9 (C_b), 126.5 (C_d), 125.7 (C_f), 125.7 (C_g), 116.1 (C_e), 113.0 (C_h), 48.7 (CH_2). ESI-TOF-MS (positive mode) for $C_{19}H_{15}N_3Cl_2Au$ ([M$^+$]): calc. 552.0309, exp. 552.0307 (err. −0.4 ppm). UV–Vis (DMSO): λ_{max} (nm) (ε, $cm^{-1}\cdot mol^{-1}\cdot dm^3$) 313 (21,527). IR (ATR): ν (cm^{-1}) 1497, 1475, 1454 ($\nu_{C–H\ stretching}$), 831, 746 ($\nu_{C=C\ bending}$).

C5. Yield 48% (265 mg, 0.351 mmol). NMR ^{1}H (DMSO-d_6): 8.80 (m, 1H, H_a), 8.31 (m, 1H, H_d), 8.17 (t, J = 5.7 Hz, 1H, H_c), 7.92–7.88 (m, 3H, 2xCH–Ph + H_e), 7.77 (m, 1H, H_h), 7.69 (m, 1H, H_b), 7.58–7.50 (m, 2H, H_f + H_g), 7.41–7.39 (m, 2H, 2xCH–Ph), 6.30 (s, 2H, CH_2), 3.80 (s, 3H, CH_3). NMR ^{13}C{^{1}H} (DMSO-d_6): 165.9 (CO_2Me), 149.9 (C_a), 145.0 (C^{IV}), 141.3 (C^{IV}), 138.3 (C_c), 134.5 (C^{IV}), 129.5 (CH–Ph), 129.1 (C^{IV}), 127.3 (CH–Ph), 126.6 (C_b), 125.9 (C_{f+g}), 125.7 (C_d), 116.5 (C_e), 112.9 (C_h), 52.2 (CH_3), 48.8 (CH_2). ESI-TOF-MS (positive mode) for $C_{21}H_{17}N_3O_2Cl_2Au$ ([M$^+$]): calc. 610.0363, exp. 610.0350 (err. −2.1 ppm). UV–Vis (DMSO): λ_{max} (nm) (ε, $cm^{-1}\cdot mol^{-1}\cdot dm^3$) 312 (23,448). IR (ATR): ν (cm^{-1}) 1706 ($\nu_{C–H\ bending}$), 1496, 1481 ($\nu_{C–H\ stretching}$), 1285, 1018 ($\nu_{C–O\ stretching}$), 1108 ($\nu_{C–N\ stretching}$), 845 ($\nu_{C=C\ bending}$).

C6. Yield: 99% (435 mg, 0.568 mmol). NMR ^{1}H (DMSO-d_6): 8.81 (d, J = 4.3 Hz, 1H, H_a), 8.32 (d, J = 7.8 Hz, 1H, H_d), 8.18 (td, J = 7.8 and 1.3 Hz, 1H, H_c), 7.92 (d, 1H, J = 7.7 Hz, H_e), 7.80 (d, 1H, J = 7.8 Hz, H_h), 7.72–7.68 (m, 3H, H_b + 2xCH–Ph), 7.59–7.53 (m, 2H, H_f + H_g), 7.52–7.49 (m, 2H, 2xCH–Ph), 6.31 (s, 2H, CH_2). NMR ^{13}C{^{1}H} (DMSO-d_6): 150.2 (C_a), 147.3 (C^{IV}), 143.9 (C^{IV}), 140.3 (C^{IV}), 138.5 (C_c), 133.6 (C^{IV}), 132.9 (C^{IV}), 128.2 (q, C^{IV}–CF_3, $^2J_{C–F}$ = 31.5 Hz), 127.9 (2xCH–Ph), 127.0 (C_b), 126.6 (C_f), 126.4 (C_g), 126.0 (C_d), 125.6 (q, 2xCH–C–CF_3, $^3J_{C–F}$ = 3.9 Hz), 123.8 (q, $C^{IV}F_3$, $^1J_{C–F}$ = 272 Hz), 115.9 (C_e), 113.2 (C_h), 48.8 (CH_2). NMR ^{19}F{^{1}H} (DMSO-d_6): −61.0 (s, CF_3), −70.0 (d, PF_6, $^1J_{P–F}$ = 712.4 Hz). ESI-TOF-MS (positive mode) for $C_{20}H_{14}N_3Cl_2F_3Au$ ([M$^+$]): calc. 620.0182, exp. 620.0212 (err. 4.8 ppm). UV–Vis (DMSO): λ_{max} (nm) (ε, $cm^{-1}\cdot mol^{-1}\cdot dm^3$) 312 (24,699). IR (ATR): ν (cm^{-1}) 1481 ($\nu_{C–H\ stretching}$), 1324, 1121, 1113 ($\nu_{C–F\ stretching}$), 1068 ($\nu_{C–N\ stretching}$), 834 ($\nu_{C=C\ bending}$). Anal. Calcd for $C_{20}H_{14}N_3Cl_2AuPF_9$ (766.18): C, 31.35; H, 1.84; N, 5.48. Found: C, 31.35; H, 1.88; N, 5.48.

C7. Yield: 87% (312 mg, 0.436 mmol). NMR ^{1}H (DMSO-d_6): 8.82 (d, J = 4.2 Hz, 1H, H_a), 8.31 (d, J = 8.0 Hz, 1H, H_d), 8.15 (t, J = 7.6 Hz, 1H, H_c), 7.86 (d, 1H, J = 7.6 Hz, H_e), 7.78 (d, 1H, J = 7.1 Hz, H_h), 7.88 (t, 1H, J = 5.3 Hz, H_b), 7.50 (m, 2H, H_f + H_g), 7.35–7.32 (m, 2H, 2xCH–Ph), 7.15–7.11 (m, 2H, 2xCH–Ph), 6.19 (s, 2H, CH_2). NMR ^{13}C{^{1}H} (DMSO-d_6): 162.9 (C^{IV}), 160.5 (C^{IV}), 150.0 (C_a), 147.4 (C^{IV}), 144.6 (C^{IV}), 138.3 (C_c), 133.9 (C^{IV}), 133.0 (d, C^{IV}F, $^1J_{C–F}$ = 203 Hz), 129.4 (d, 2xCH–Ph, $^3J_{C–F}$ = 8.4 Hz), 126.7 (C_b), 126.0 (C_f), 126.0 (C_g), 125.9 (C_d), 116.3 (C_e), 115.6 (d, 2xCH–Ph, $^2J_{C–F}$ = 21.5 Hz), 113.1 (C_h), 48.2 (CH_2). NMR ^{19}F{^{1}H} (DMSO-d_6): −114.3 (s, Ph–F), −70.0 (d, PF_6, $^1J_{P–F}$ = 711.9 Hz). ESI-TOF-MS (positive mode) for $C_{19}H_{14}N_3Cl_2FAu$ ([M$^+$]): calc. 570.0214, exp. 570.0236 (err. 3.9 ppm). UV–Vis (DMSO): λ_{max} (nm) (ε, $cm^{-1}\cdot mol^{-1}\cdot dm^3$) 312 (25,542). IR (ATR): ν (cm^{-1}) 1460 ($\nu_{C–H\ stretching}$),

1232 ($\nu_{C-F\ stretching}$), 835 ($\nu_{C=C\ bending}$). Anal. Calcd for $C_{18}H_{12}N_3O_2Cl_2AuPF_7$ (702.14): C, 31.86; H, 1.97; N, 5.87. Found: C, 31.82; H, 2.00; N, 5.88.

C8. Yield: 99% (394 mg, 0.500 mmol). NMR ^{1}H (DMSO-d_6): 8.76 (d, J = 4.4 Hz, 1H, H_a), 8.31 (d, J = 7.9 Hz, 1H, H_d), 8.14 (td, J = 7.8 and 1.6 Hz, 1H, H_c), 7.90–7.86 (m, 2H, H_h + H_e), 7.66 (m, 1H, H_b), 7.58–7.51 (m, 2H, H_f + H_g), 6.36 (s, 2H, CH_2). NMR ^{13}C{^{1}H} (DMSO-d_6): 149.3 (C_a), 148.5 (C^{IV}), 146.7 (C^{IV}), 146.0 (dd, C^{IV}F, $^1J_{C-F}$ = 246 Hz), 138.3 (C_c), 137.1 (C^{IV}), 135.2 (C^{IV}), 126.0 (C_b), 125.4 (C_g), 125.3 (C_f), 125.0 (C_d), 117.9 (C_e), 112.1 (C_h), 110.9 (t, C^{IV}–Ph, $^2J_{C-F}$ = 17 Hz), 39.9 (CH_2). NMR ^{19}F{^{1}H} (DMSO-d_6): −141.9 (Ph–*F*), −154.3 (Ph–*F*), −162.4 (Ph–*F*), −70.0 (d, PF_6, $^1J_{P-F}$ = 711.9 Hz). ESI-TOF-MS (positive mode) for $C_{19}H_{10}N_3Cl_2F_5Au$ ([M$^+$]): calc. 641.9837, exp. 641.9874 (err. 5.8 ppm). UV–Vis (DMSO): λ_{max} (nm) (ε, cm^{-1}·mol^{-1}·dm^3) 311 (23,441). IR (ATR): ν (cm^{-1}) 1474 ($\nu_{C-H\ stretching}$), 1337, 1128 ($\nu_{C-F\ stretching}$), 1029 ($\nu_{C-N\ stretching}$), 838 ($\nu_{C=C\ bending}$).

C9. Yield: 99% (443 mg, 0.603 mmol). NMR ^{1}H (DMSO-d_6): 8.82 (d, J = 4.2 Hz, 1H, H_a), 8.29 (d, J = 8.0 Hz, 1H, H_d), 8.20 (t, J = 7.6 Hz, 1H, H_c), 7.91 (d, 1H, J = 7.6 Hz, H_e), 7.78 (d, 1H, J = 7.1 Hz, H_h), 7.88 (t, 1H, J = 5.3 Hz, H_b), 7.57 (m, 2H, H_f + H_g), 7.19–7.09 (m, 4H, 4xC*H*–Ph), 6.20 (s, 2H, CH_2). NMR ^{13}C{^{1}H} (DMSO-d_6): 162.6 (d, C^{IV}F, $^1J_{C-F}$ = 247 Hz), 162.4 (d, C^{IV}F, $^1J_{C-F}$ = 247 Hz), 150.2 (C_a), 147.2 (C^{IV}), 143.6 (C^{IV}), 139.9 (t, C^{IV}Ph, $^3J_{C-F}$ = 9.6 Hz), 138.5 (C_c), 133.4 (C^{IV}), 132.4 (C^{IV}), 127.1 (C_b), 126.7, 126.5 (C_f, C_g), 126.1 (C_d), 115.7 (C_e), 113.2 (C_h), 110.6 (d, 2x*C*H–Ph, $^2J_{C-F}$ = 26.1 Hz), 103.5 (t, *C*H–Ph, $^2J_{C-F}$ = 25.8 Hz), 48.5 (CH_2). NMR ^{19}F{^{1}H} (DMSO-d_6): −109.1 (s, 2xPh–*F*), −70.0 (d, PF_6, $^1J_{P-F}$ = 712.6 Hz). ESI-TOF-MS (positive mode) for $C_{19}H_{13}N_3Cl_2F_2Au$ ([M$^+$]): calc. 588.0120, exp. 588.0150 (err. 5.1 ppm). UV–Vis (DMSO): λ_{max} (nm) (ε, cm^{-1}·mol^{-1}·dm^3) 313 (14,367). IR (ATR): ν (cm^{-1}) 1442 ($\nu_{C-H\ stretching}$), 1332, 1091 ($\nu_{C-F\ stretching}$), 1039 ($\nu_{C-N\ stretching}$), 833, 792 ($\nu_{C=C\ bending}$).

3.2.3. General Procedure for the Synthesis of the Neutral Complexes **C10**–**C12**

The synthesis of complex **C10** was already reported by us [15] and others [19], and was adapted to the synthesis of **C11** and **C12**. To a solution of 1 eq. of pyridylbenzimidazole ligand **L10**–**L12** in acetonitrile (1 mL) was added an aqueous solution of 1 eq. of KOH in water (6 mL). The reaction mixture was stirred at room temperature for 15 min. An aqueous solution of 1 eq. of $NaAuCl_4$ (6 mL) was then added, and the resulting mixture was stirred overnight at room temperature. The resulting dark brown precipitate was filtered; washed with water, ethanol and diethyl ether; and dried under vacuum.

C11. Yield: 57% (100 mg, 0.18 mmol). NMR ^{1}H (500 MHz, DMSO-d_6): 9.11–8.90 (m, 3H, 3xC*H*), 8.78 (m, 1H, C*H*), 8.42 (m, 2H, 2xC*H*), 8.21 (m, 1H, C*H*), 8.13 (m, 1H, C*H*), 7.86–7.74 (m, 3H, 3xC*H*), 7.67 (m, 1H, C*H*). NMR ^{13}C{^{1}H} (125.77 MHz, DMSO-d_6): 160.8 (C^{IV}), 150.3 (CH), 145.4 (C^{IV}), 145.0 (C^{IV}), 138.0 (CH), 134.9 (C^{IV}), 128.8 (CH), 127.6 (CH), 127.4 (CH), 125.5 (CH), 124.6 (CH), 124.5 (CH), 123.4 (CH), 122.7 (CH), 122.5 (CH), 121.0 (CH), 120.4 (CH). ESI-TOF-MS (positive mode) for $C_{20}H_{12}N_3ClAu$ ([M − Cl$^+$]): calc. 526.0385, exp. 526.0386 (err. 0.2 ppm). UV–Vis (DMSO): λ_{max} (nm) (ε, cm^{-1}·mol^{-1}·dm^3) 333 (20,891), 362 (16,528). IR (ATR): ν (cm^{-1}) 1428, 1452 ($\nu_{C-H\ stretching}$), 1034 ($\nu_{C-N\ stretching}$), 774 ($\nu_{C=C\ bending}$).

C12. Yield: 47% (87 mg, 0.15 mmol). NMR ^{1}H (500 MHz, MeCN-d_3): 8.63–8.47 (m, C*H*), 8.35 (m, C*H*), 8.27 (m, C*H*), 8.23 (m, C*H*), 8.14–7.98 (m, C*H*), 7.59–7.57 (m, C*H*). NMR ^{13}C{^{1}H} (125.77 MHz, DMSO-d_6): 161.2 (C^{IV}), 150.4 (CH), 149.6 (CH), 145.7 (C^{IV}), 145.5 (C^{IV}), 138.0 (CH), 135.6 (C^{IV}), 131.7 (C^{IV}), 128.3 (CH), 127.8 (CH), 127.2 (CH), 126.6 (CH), 125.0 (CH), 124.5 (C^{IV}), 123.4 (CH), 122.8 (C^{IV}), 122.6 (C^{IV}), 122.2 (C^{IV}), 120.0 (CH), 119.7 (CH), 119.5 (C^{IV}), 118.3 (CH). ESI-TOF-MS (positive mode) for $C_{22}H_{12}N_3ClAu$ ([M − Cl$^+$]): calc. 550.0385, exp. 550.0393 (err. 1.5 ppm). UV–Vis (DMSO): λ_{max} (nm) (ε, cm^{-1}·mol^{-1}·dm^3) 338 (28,904), 353 (28,264), 366 (19,892), 388 (20,031). IR (ATR): ν (cm^{-1}) 1442 ($\nu_{C-H\ stretching}$), 1064 ($\nu_{C-N\ stretching}$), 738 ($\nu_{C=C\ bending}$).

3.3. UV–Visible and Fluorescence Spectroscopy

The data are reported as the absorption maximum wavelength (λ_{max}, in nm) and corresponding molar extinction coefficient at λ_{max} (ε, in L·mol^{-1}·cm^{-1}). Macro quartz cuvettes with a path length of 1 cm were used. The sample concentrations were chosen to obtain a maximum absorbance of around

0.8 to then measure the quantum yields. Relative quantum yields of fluorescence of the samples were obtained by comparing the areas under the corrected emission spectra with a standard absorbing in the same region than the sample. Measurements were performed in degassed DMSO (Sigma-Aldrich, spectroscopic grade ≥99.9%) at 298 K. Quinine sulfate (Φ_F = 0.546 in 0.5 M H_2SO_4, λ_{ex} = 366 nm) was used as the standard [26]. In all Φ_F calculations, the correction for the solvent refractive index (η) was applied: DMSO: η = 1.479; H_2O (or H_2SO_4): η = 1.333 [27]. The following equation was used to calculate the quantum yield of the sample ($\Phi_{F,x}$), in which $\Phi_{F,St}$ is the reported quantum yield of the standard, *F* is the integral photon flux, *f* is the absorption factor, and η is the refractive index of the solvent used. The *x* subscript denotes the sample, and *St* denotes the standard, and the fluorescence spectra between the sample and the standard were recorded at the same λ_{ex} [28]:

$$\Phi_{F,x} = \Phi_{F,St} \cdot \frac{F_x}{F_{St}} \cdot \frac{f_{St}}{f_x} \cdot \frac{\eta_x^2}{\eta_{St}^2}$$

3.4. X-ray Diffraction Analysis

Complexes **C6** and **C7** were allowed to form crystals by slow diffusion of pentane into a corresponding complex's concentrated solution in a mixture of acetonitrile and dicholoromethane at room temperature. The crystals were analysed at the UK National Crystallography Service in Southampton [29]. A suitable yellow block-shaped crystal from **C6** (0.050 × 0.040 × 0.030) mm^3 and from **C7** (0.080 × 0.050 × 0.020) mm^3, were selected and mounted on a MITIGEN holder in perfluoroether oil and mounted on a Rigaku 007HF diffractometer equipped with Varimax confocal mirrors and an AFC11 goniometer and HyPix 6000HE detector. The crystals were kept at *T* = 100.00(10) K during data collection. Using *Olex2* [30], the structures were solved with the *ShelXT* [31] structure solution program, using the Intrinsic Phasing solution method. The models were refined with version 2014/7 of *ShelXL* [32] using Least Squares minimisation, and the ORTEP views are presented in Figures S62 and S63. (CCDC 1868645 and 1868642 contain the supplementary crystallographic data for this paper. These data can be obtained free of charge via http://www.ccdc.cam.ac.uk/conts/retrieving.html (or from the CCDC, 12 Union Road, Cambridge CB2 1EZ, UK; Fax: +44 1223 336033; E-mail: deposit@ccdc.cam.ac.uk)).

3.5. UV–Visible Absorption Spectroscopy

The new Au(III) complexes were tested for their stability in aqueous media (1× Phosphate Buffer Saline (PBS, Corning), pH 7.4) in the presence or absence of 2 eq. GSH (vs. 1 eq. of Au(III) complex). The solutions were prepared from a stock solution of the Au(III) complex at a concentration of 10^{-2} M in DMSO and diluted to reach a concentration of 10^{-4} M in PBS. The absorption spectra were recorded over time at room temperature using a Cary 500 UV–Visible NIR spectrophotometer.

3.6. Aquaporins Inhibition

Venous blood samples were obtained from healthy human volunteers following a protocol approved by the Ethics Committee of the Faculty of Pharmacy of the University of Lisbon (Instituto Português de Sangue Protocol SN-22/05/2007). Informed written consent was obtained from all participants. Blood samples, collected in citrate anticoagulant (2.7% citric acid, 4.5% trisodium citrate and 2% glucose), were centrifuged at 750× *g* for 5 min at 4 °C. Plasma and buffy coat were discarded. Pelleted erythrocytes were washed three times in PBS (KCl 2.7 mM, KH_2PO_4 1.76 mM, Na_2HPO_4 10.1 mM, NaCl 137 mM, pH 7.4), diluted to 0.5% haematocrit and immediately used for experiments. hRBC mean volume in isotonic solution was determined using a CASY-1 Cell Counter (Schärfe System GmbH, Reutlingen, Germany) and was calculated as 82 fL. Stopped-flow experiments were performed on a HI-TECH Scientific PQ/SF-53 apparatus, with 2 ms dead time, temperature controlled and were interfaced with a microcomputer. Measurements of water permeability (Pf) and glycerol permeability (Pgly) were performed as described in References [12,33]. Briefly, 100 μL of

the suspension of fresh erythrocytes (0.5%) was mixed with an equal volume of hyperosmotic PBS containing 200 mM sucrose (a non-permeable osmolyte that induces water outflow and subsequent cell shrinkage) and 200 mM glycerol (a permeable osmolyte that induces first fast cell shrinkage due to water outflow and then glycerol influx in response to its chemical gradient, followed by water influx with subsequent cell reswelling). The kinetics of cell volume change were measured from the time course of 90° scattered light intensity at 400 nm until a stable light scatter signal was attained. For each experimental condition, 5–7 replicates were analysed. Pf was estimated by Pf = k (Vo/A)(1/Vw(osm_{out})∞), where Vw is the molar volume of water, Vo/A is the initial cell volume to area ratio, (osm_{out})∞ is the final medium osmolarity after the applied osmotic gradient, and k is the single exponential time constant fitted to the light scattering signal of erythrocyte shrinkage. Pgly was estimated by Pgly = k (Vo/A), where k is the single exponential time constant fitted to the light scattering signal of glycerol influx in erythrocytes.

In inhibition experiments, cells were incubated with different concentrations of complexes from freshly prepared stock solutions, for 30 min at r.t. before stopped-flow experiments. A time-dependent inhibition assay for all the tested compounds over several hours of incubation showed no further increase of inhibition after 30 min at r.t. The inhibitor concentration necessary to achieve 50% inhibition (IC_{50}) was calculated by nonlinear regression of the dose-response curves (Graph Pad Prism, Inc, San Diego, CA, USA) to the equation: $y = y_{min} + (y_{max} - y_{min})/(1 + 10((LogIC_{50} - Log[Inh])H))$, where y is the percentage inhibition obtained for each concentration of inhibitor [Inh], and H is the Hill slope. All solution osmolarities were determined from freezing point depression on a semi-micro osmometer (Knauer GmbH, Berlin, Germany) using standards of 100 and 400 mOsM.

3.7. Cell Lines and Culture Conditions

Human cell lines of lung adenocarcinoma (A549), breast carcinoma (MCF-7), ovarian adenocarcinoma (SKOV-3) and skin malignant melanoma (A375) were obtained from American Type Culture Collection (ATCC). The cells were cultured in Dulbecco's Modified Eagle Medium (DMEM, 4.5 g/L glucose, Corning, Thermo Fisher Scientific), supplemented with 10% foetal bovine serum (One-Shot FBS, EU-approved South American Origin, Thermo Fisher Scientific) and 1% penicillin/streptomycin (Gibco). All cell lines were cultured at 37 °C, in a humidified atmosphere of 5% CO_2 and passaged when reaching confluence.

3.8. Immunocytofluorescence

Round glass coverslips (Ø 13mm, VWR) sterilized by UV-light exposure were inserted in 24-well tissue culture-treated plates (Corning) prior to the addition of cells. Cells were seeded at a concentration of 125,000 cells/mL and incubated at 37 °C under humidified atmosphere with 5% CO_2, for 24 h. Glass coverslips were removed from the wells and washed three times with 1× PBS (Gibco). Afterwards, cells were fixed for 20 min with 4% formaldehyde (Alfa Aesar) and permeabilized for 5 min with 0.2% Triton X-100 (Alfa Aesar) at room temperature (r.t.). Glass coverslips were then incubated with 1:500 primary anti-AQP3 antibody (rabbit anti-human, PA1488 BosterBio, Pleasanton, CA, USA) in 1× PBS with 5% normal human serum (NHS, Invitrogen, UK), for 1 h at r.t., followed by incubation with 1:500 secondary goat anti-rabbit Alexa Fluor®488 (ab150077, Abcam, Cambridge, MA, US), in 1× PBS with 5% NHS for 1 h, at r.t. and in the dark. Before/after each step, cells were washed thrice with 1× PBS. After removing excess PBS, cells were mounted on glass microscope slides (VWR) using Mowiol® 4–88 (Sigma-Aldrich). Images were acquired on a Zeiss Axio Vert.A1 microscope and processed using Fiji (ImageJ) [34].

3.9. Flow Cytometry Analysis

For flow cytometry evaluation of AQP3 expression, samples of each cell line studied were prepared with 200,000 cells/sample. Cells were initially washed twice with 1× PBS (Gibco) and subsequently fixed with 4% formaldehyde (Alfa Aesar) for 30 min at room temperature (r.t.). Afterwards, cells were

incubated with 1:500 dilution of anti-AQP3 antibody (rabbit anti-human, PA1488 Boster), in 1× PBS with 5% normal human serum (NHS, Invitrogen) and 0.1% Triton X-100 (Alfa Aesar) at r.t., for 1 h. Staining with primary antibody was followed by incubation with 1:500 secondary goat anti-rabbit Alexa Fluor®488 (ab150077, Abcam), in 1× PBS with 5% NHS and 0.1% Triton X-100 also for 1 h and at r.t., in the dark. Cells were kept on ice and away from direct light until analysed using a BD FACS Verse Flow Cytometer. Results were analysed using FlowJo 10.5.0. Firstly, samples were gated for live cells. Afterwards, stained and unstained samples were compared, in order to gate the positive population and the mean fluorescence, intensity (geometric mean) was taken from each positive sample peak. Data were normalized for the sample with the lowest AQP3 expression and results are shown as mean ± SEM of three independent experiments.

3.10. Antiproliferative Activities

For evaluation of cell growth inhibition, cells were seeded in 96-well plates (Corning) at a concentration of 15,000 cells/well, grown for 24 h in 200 µL complete medium. Solutions of the samples with the desired concentration (1 to 100 µM) were prepared by diluting a freshly prepared stock solution (10^{-2} M in DMSO) of the corresponding compound in aqueous DMEM medium, accordingly. Auphen (stock solution 10 mM in DMSO) was used as the reference compound. A negative control (medium only) was run for all the assays. After 24 h incubation, 200 µL of the compounds' dilutions were added to each well, and cells were incubated for an additional 72 h. Afterwards, medium was removed and 3-(4,5-dimethylthiazol-2-yl)-2,5-diphenyltetrazolium bromide (MTT, Fluorochem) in 10× PBS (Corning) was added to the cells, at a final concentration of 0.3 mg/mL, and incubated for 3–4 h. After, the MTT solution was discarded and replaced with DMSO, to allow the formed violet formazan crystals to dissolve. The optical density was quantified in quadruplicates for each experiment, at 550 nm using a multi-well plate reader (VICTOR X, Perking Elmer, UK). The percentage of surviving cells was calculated from the ratio of absorbance of treated to untreated cells. The EC_{50} values were calculated, using GraphPad Prism software, as the concentration showed 50% decrease in cell viability, compared to controls, using a nonlinear fit of concentration *vs.* response. Data is presented as mean ±SEM of at least three independent experiments.

4. Conclusions

In conclusion, we have synthesized a new series of Au(III) compounds, cationic and neutral, featuring a pyridine-benzimidazole scaffold, which has been characterized via different methods. Varying the ligands' substitution patterns influences the stability of the resulting Au(III) complexes in aqueous environment, as demonstrated by UV–visible spectroscopy. In general, all the compounds promptly react with the reducing agent GSH, except **C11**–**C12**. All the new gold-based complexes are potent inhibitors of human water and glycerol channel aqualgyceoroporin-3 (AQP3), while they are inactive as inhibitors of the water channel AQP1, as evidenced by stopped-flow spectroscopy in hRBC. While most of the compounds are scarcely active as antiproliferative agents against human cancer cells, the neutral complexes **C10**–**C12** showed promising anticancer activities, particularly in the melanoma A375 cancer cell line. Interestingly, while all the selected cell lines express AQP3, the melanoma cells display protein expression also at the level of the nuclear membrane, as shown by immunocytofluorescence. Thus, it may be hypothesized that **C10**–**C12** targets mainly AQP3 in the nuclear membrane after being taken up by the cancer cells. Overall, our results hold promise for the design of novel selective AQPs inhibitors to be used anticancer agents or as chemical probes to study the function of these interesting membrane channels.

Supplementary Materials: The following are available online at http://www.mdpi.com/2304-6740/6/4/123/s1, CIF and checkCIF files. Scheme S1: Synthetic pathways to ligands **L1**–**L12**. Figure S1: ^{1}H NMR (400.13 MHz, $CDCl_3$) spectrum of ligand **L5**. Figure S2: $^{13}C\{^{1}H\}$ NMR (100.61 MHz, $CDCl_3$) spectrum of ligand **L5**. Figure S3: ^{1}H NMR (400.14 MHz, $CDCl_3$) spectrum of ligand **L6**. Figure S4: ^{13}C{1H} NMR (100.61 MHz, $CDCl_3$) spectrum of ligand **L6**. Figure S5: ^{1}H NMR (500.13 MHz, DMSO-d_6) spectrum of complex **C2**. Figure S6: $^{13}C\{^{1}H\}$ NMR

(125.77 MHz, DMSO-d_6) spectrum of complex **C2**. Figure S7: ^{1}H NMR (400.13 MHz, DMSO-d_6) spectrum of complex **C3**. Figure S8: ^{13}C{^{1}H} NMR (125.77 MHz, DMSO-d_6) spectrum of complex **C3**. Figure S9: ^{1}H NMR (400.13 MHz, DMSO-d_6) spectrum of complex **C4**. Figure S10: ^{13}C{^{1}H} NMR (125.77 MHz, DMSO-d_6) spectrum of complex **C4**. Figure S11: ^{1}H NMR (400.13 MHz, DMSO-d_6) spectrum of complex **C5**. Figure S12: ^{13}C{^{1}H} NMR (100.61 MHz, DMSO-d_6) spectrum of complex **C5**. Figure S13: ^{1}H NMR (400.13 MHz, DMSO-d_6) spectrum of complex **C6**. Figure S14: ^{13}C{^{1}H} NMR (100.61 MHz, DMSO-d_6) spectrum of complex **C6**. Figure S15: ^{1}H NMR (400.13 MHz, DMSO-d_6) spectrum of complex **C7**. Figure S16: ^{13}C{^{1}H} NMR (100.61 MHz, DMSO-d_6) spectrum of complex **C7**. Figure S17: ^{1}H NMR (400.13 MHz, DMSO-d_6) spectrum of complex **C8**. Figure S18: ^{13}C{^{1}H} NMR (100.61 MHz, DMSO-d_6) spectrum of complex **C8**. Figure S19: ^{1}H NMR (400.13 MHz, DMSO-d_6) spectrum of complex **C9**. Figure S20: ^{13}C{^{1}H} NMR (100.61 MHz, DMSO-d_6) spectrum of complex **C9**. Figure S21: ^{1}H NMR (500.17 MHz, DMSO-d_6) spectrum of complex **C11**. Figure S22: ^{13}C{^{1}H} NMR (125.77 MHz, DMSO-d_6) spectrum of complex **C11**. Figure S23: ^{1}H NMR (500.17 MHz, MeCN-d_3) spectrum of complex **C12**. Figure S24: ^{13}C{^{1}H} NMR (125.77 MHz, DMSO-d_6) spectrum of complex **C12**. Figure S25: Absorption and emission spectra of ligand **L1**. Figure S26: Absorption and emission spectra of complex **C1**. Figure S27: Absorption and emission spectra of ligand **L2**. Figure S28: Absorption and emission spectra of complex **C2**. Figure S29: Absorption and emission spectra of ligand **L3**. Figure S30: Absorption and emission spectra of complex **C3**. Figure S31: Absorption and emission spectra of ligand **L4**. Figure S32: Absorption and emission spectra of complex **C4**. Figure S33: Absorption and emission spectra of ligand **L5**. Figure S34: Absorption and emission spectra of complex **C5**. Figure S35: Absorption and emission spectra of ligand **L6**. Figure S36: Absorption and emission spectra of complex **C6**. Figure S37: Absorption and emission spectra of ligand **L7**. Figure S38: Absorption and emission spectra of complex **C7**. Figure S39: Absorption and emission spectra of ligand **L8**. Figure S40: Absorption and emission spectra of complex **C8**. Figure S41: Absorption and emission spectra of ligand **L9**. Figure S42: Absorption and emission spectra of complex **C9**. Figure S43: Absorption and emission spectra of ligand **L10**. Figure S44: Absorption and emission spectra of complex **C10**. Figure S45: Absorption and emission spectra of ligand **L11**. Figure S46: Absorption and emission spectra of complex **C11**. Figure S47: Absorption and emission spectra of ligand **L12**. Figure S48: Absorption and emission spectra of complex **C12**. Figure S49: UV–Visible spectra of the Au(III) complex **C1** (10^{-4} M) in PBS (pH 7.4) recorded over time (left); and of **C1** before and after addition of GSH (2 eq.) recorded over time at room temperature (right). Figure S50: UV–Visible spectra of the Au(III) complex **C2** (10^{-4} M) in PBS (pH 7.4) recorded over time (left); and of **C2** before and after addition of GSH (2 eq.) recorded over time at room temperature (right). Figure S51: UV–Visible spectra of the Au(III) complex **C3** (10^{-4} M) in PBS (pH 7.4) recorded over time (left); and of **C3** before and after addition of GSH (2 eq.) recorded over time at room temperature (right). Figure S52: UV–Visible spectra of the Au(III) complex **C4** (10^{-4} M) in PBS (pH 7.4) recorded over time (left); and of **C4** before and after addition of GSH (2 eq.) recorded over time at room temperature (right). Figure S53: UV–Visible spectra of the Au(III) complex **C5** (10^{-4} M) in PBS (pH 7.4) recorded over time (left); and of **C5** before and after addition of GSH (2 eq.) recorded over time at room temperature (right). Figure S54: UV–Visible spectra of the Au(III) complex **C**6 (10^{-4} M) in PBS (pH 7.4) recorded over time (left); and of **C6** before and after addition of GSH (2 eq.) recorded over time at room temperature (right). Figure S55: UV–Visible spectra of the Au(III) complex **C7** (10^{-4} M) in PBS (pH 7.4) recorded over time (left); and of **C7** before and after addition of GSH (2 eq.) recorded over time at room temperature (right). Figure S56: UV–Visible spectra of the Au(III) complex C8 (10^{-4} M) in PBS (pH 7.4) recorded over time (left); and of **C8** before and after addition of GSH (2 eq.) recorded over time at room temperature (right). Figure S57: UV–Visible spectra of the Au(III) complex **C9** (10^{-4} M) in PBS (pH 7.4) recorded over time (left); and of **C9** before and after addition of GSH (2 eq.) recorded over time at room temperature (right). Figure S58: UV–Visible spectra of the Au(III) complex **C10** (10^{-4} M) in PBS (pH 7.4) recorded over time (left); and of **C10** before and after addition of GSH (2 eq.) recorded over time at room temperature (right). Figure S59: UV–Visible spectra of the Au(III) complex **C11** (10^{-4} M) in PBS (pH 7.4) recorded over time (left); and of **C11** before and after addition of GSH (2 eq.) recorded over time at room temperature (right). Figure S60: UV–Visible spectra of the Au(III) complex **C12** (10^{-4} M) in PBS (pH 7.4) recorded over time (left); and of **C12** before and after addition of GSH (2 eq.) recorded over time at room temperature (right). Figure S61: Normalized mean fluorescence intensity (MFI) of AQP3, detected using a secondary Alexa Fluor®488-labelled antibody. Results were normalized for the sample with the lowest expression (A375) and results are expressed as mean ±SEM of three independent experiments. * $p < 0.03$. Figure S62: X-ray structure of crystals of **C6**. Thermal ellipsoids drawn at the 50% probability level. Figure S63: X-ray structure of crystals of **C7**. Thermal ellipsoids drawn at the 50% probability level. Table S1: Antiproliferative activities (EC_{50} values) of ligands in human SKOV-3, A375, MCF-7, and A549 cells after 72 h incubation.

Author Contributions: Conceptualization, A.C. and G.S.; methodology, M.N.W., A.C., A.d.A., A.M., G.S.; formal analysis, A.M., A.d.A., B.A.; investigation, B.A., M.N.W., A.d.A., A.M.; resources, A.C. and G.S.; data curation, M.N.W., B.A., A.d.A., A.M.; X-ray data acquisition and analysis, W.T.K. and S.J.C; writing—original draft preparation, A.C., M.N.W.; writing—review and editing, all authors; visualization, B.A., A.d.A., A.M.; supervision, A.C., G.S.; funding acquisition, A.C., G.S.

Funding: This research received no external funding.

Acknowledgments: Cardiff University and Fundação para a Ciência e Tecnologia, Portugal (project PTDC/BTM-SAL/28977/2017 and PhD fellowship to A.M. SFRH/BD/52384/2013) are acknowledged for funding.

Conflicts of Interest: The authors declare no conflict of interest.

References

1. Casini, A.; Sun, R.W.-Y.; Ott, I. Medicinal Chemistry of Gold Anticancer Metallodrugs. In *Metallo-Drugs: Development and Action of Anticancer Agents*; Sigel, A., Sigel, H., Freisinger, E., Sigel, R.K.O., Eds.; De Gruyter: Berlin, Germany; Boston, MA, USA, 2018; pp. 199–217.
2. Shaw, C.F. Gold-based therapeutic agents. *Chem. Rev.* **1999**, *99*, 2589–2600. [CrossRef]
3. De Almeida, A.; Oliveira, B.L.; Correia, J.D.G.; Soveral, G.; Casini, A. Emerging protein targets for metal-based pharmaceutical agents: An update. *Coord. Chem. Rev.* **2013**, *257*, 2689–2704. [CrossRef]
4. de Almeida, A.; Soveral, G.; Casini, A. Gold compounds as aquaporin inhibitors: New opportunities for therapy and imaging. *Med. Chem. Commun.* **2014**, *5*, 1444–1453. [CrossRef]
5. Agre, P. Aquaporin Water Channels (Nobel Lecture). *Angew. Chem. Int. Ed.* **2004**, *43*, 4278–4290. [CrossRef] [PubMed]
6. Verkman, A.S. More than just water channels: Unexpected cellular roles of aquaporins. *J. Cell Sci.* **2005**, *118*, 3225–3232. [CrossRef] [PubMed]
7. Soveral, G.; Nielsen, S.; Casini, A. *Aquaporins in Health and Disease: New Molecular Targets for Drug Discovery*, 1st ed.; Soveral, G., Nielsen, S., Casini, A., Eds.; CRC Press: Boca Raton, FL, USA, 2016; ISBN 978-971-4987-0783-1.
8. Madeira, A.; Fernández-Veledo, S.; Camps, M.; Zorzano, A.; Moura, T.F.; Ceperuelo-Mallafré, V.; Vendrell, J.; Soveral, G. Human Aquaporin-11 is a water and glycerol channel and localizes in the vicinity of lipid droplets in human adipocytes. *Obesity* **2014**, *22*, 2010–2017. [CrossRef] [PubMed]
9. Ishibashi, K.; Tanaka, Y.; Morishita, Y. The role of mammalian superaquaporins inside the cell. *Biochim. Biophys. Acta Gen. Subj.* **2014**, *1840*, 1507–1512. [CrossRef] [PubMed]
10. Aikman, B.; De Almeida, A.; Meier-Menches, S.M.; Casini, A. Aquaporins in cancer development: Opportunities for bioinorganic chemistry to contribute novel chemical probes and therapeutic agents. *Metallomics* **2018**, *10*, 696–712. [CrossRef] [PubMed]
11. Soveral, G.; Casini, A. Aquaporin modulators: A patent review (2010–2015). *Expert Opin. Ther. Pat.* **2017**, *27*, 49–62. [CrossRef] [PubMed]
12. Martins, A.P.; Marrone, A.; Ciancetta, A.; Cobo, A.G.; Echevarría, M.; Moura, T.F.; Re, N.; Casini, A.; Soveral, G. Targeting aquaporin function: Potent inhibition of aquaglyceroporin-3 by a gold-based compound. *PLoS ONE* **2012**, *7*, e37435. [CrossRef] [PubMed]
13. Martins, A.P.; Ciancetta, A.; deAlmeida, A.; Marrone, A.; Re, N.; Soveral, G.; Casini, A. Aquaporin inhibition by gold(III) compounds: New insights. *ChemMedChem* **2013**, *8*, 1086–1092. [CrossRef] [PubMed]
14. Serna, A.; Galán-Cobo, A.; Rodrigues, C.; Sánchez-Gomar, I.; Toledo-Aral, J.J.; Moura, T.F.; Casini, A.; Soveral, G.; Echevarría, M. Functional Inhibition of Aquaporin-3 With a Gold-Based Compound Induces Blockage of Cell Proliferation. *J. Cell. Physiol.* **2014**, *229*, 1787–1801. [CrossRef] [PubMed]
15. de Almeida, A.; Mósca, A.F.; Wragg, D.; Wenzel, M.; Kavanagh, P.; Barone, G.; Leoni, S.; Soveral, G.; Casini, A. The mechanism of aquaporin inhibition by gold compounds elucidated by biophysical and computational methods. *Chem. Commun.* **2017**, *53*, 3830–3833. [CrossRef] [PubMed]
16. Murray, M.; Ryan, A.J.; Little, P.J. Inhibition of rat hepatic microsomal aminopyrine N-demethylase activity by benzimidazole derivatives. Quantitative structure-activity relationships. *J. Med. Chem.* **1982**, *25*, 887–892. [CrossRef] [PubMed]
17. Sontakke, V.A.; Ghosh, S.; Lawande, P.P.; Chopade, B.A.; Shinde, V.S. A simple, efficient synthesis of 2-aryl benzimidazoles using silica supported periodic acid catalyst and evaluation of anticancer activity. *ISRN Org. Chem.* **2013**, *2013*. [CrossRef] [PubMed]
18. Prosser, K.E.; Chang, S.W.; Saraci, F.; Le, P.H.; Walsby, C.J. Anticancer copper pyridine benzimidazole complexes: ROS generation, biomolecule interactions, and cytotoxicity. *J. Inorg. Biochem.* **2017**, *167*, 89–99. [CrossRef] [PubMed]

19. Serratrice, M.; Cinellu, M.A.; Maiore, L.; Pilo, M.; Zucca, A.; Gabbiani, C.; Guerri, A.; Landini, I.; Nobili, S.; Mini, E.; et al. Synthesis, structural characterization, solution behavior, and in vitro antiproliferative properties of a series of gold complexes with 2-(2′-pyridyl)benzimidazole as ligand: Comparisons of gold(III) versus gold(I) and mononuclear versus binuclear derivat. *Inorg. Chem.* **2012**, *51*, 3161–3171. [CrossRef] [PubMed]
20. Gümüş, F.; Pamuk, İ.; Özden, T.; Yıldız, S.; Diril, N.; Öksüzoğlu, E.; Gür, S.; Özkul, A. Synthesis, characterization and in vitro cytotoxic, mutagenic and antimicrobial activity of platinum(II) complexes with substituted benzimidazole ligands. *J. Inorg. Biochem.* **2003**, *94*, 255–262. [CrossRef]
21. Huang, W.-K.; Cheng, C.-W.; Chang, S.-M.; Lee, Y.-P.; Diau, E.W.-G. Synthesis and electron-transfer properties of benzimidazole-functionalized ruthenium complexes for highly efficient dye-sensitized solar cells. *Chem. Commun.* **2010**, *46*, 8992–8994. [CrossRef] [PubMed]
22. Mardanya, S.; Karmakar, S.; Das, S.; Baitalik, S. Anion and cation triggered modulation of optical properties of a pyridyl-imidazole receptor rigidly linked to pyrene and construction of INHIBIT, OR and XOR molecular logic gates: A combined experimental and DFT/TD-DFT investigation. *Sens. Actuators B Chem.* **2015**, *206*, 701–713. [CrossRef]
23. Petryszak, R.; Keays, M.; Tang, Y.A.; Fonseca, N.A.; Barrera, E.; Burdett, T.; Füllgrabe, A.; Fuentes, A.M.-P.; Jupp, S.; Koskinen, S.; et al. Expression Atlas update—An integrated database of gene and protein expression in humans, animals and plants. *Nucleic Acids Res.* **2016**, *44*, D746–D752. [CrossRef] [PubMed]
24. Fulmer, G.R.; Miller, A.J.M.; Sherden, N.H.; Gottlieb, H.E.; Nudelman, A.; Stoltz, B.M.; Bercaw, J.E.; Goldberg, K.I. NMR chemical shifts of trace impurities: Common laboratory solvents, organics, and gases in deuterated solvents relevant to the organometallic chemist. *Organometallics* **2010**, *29*, 2176–2179. [CrossRef]
25. Cao, Q.; Bailie, D.S.; Fu, R.; Muldoon, M.J. Cationic palladium(II) complexes as catalysts for the oxidation of terminal olefins to methyl ketones using hydrogen peroxide. *Green Chem.* **2015**, *17*, 2750–2757. [CrossRef]
26. Sunesh, C.D.; Mathai, G.; Choe, Y. Constructive Effects of Long Alkyl Chains on the Electroluminescent Properties of Cationic Iridium Complex-Based Light-Emitting Electrochemical Cells. *ACS Appl. Mater. Interfaces* **2014**, *6*, 17416–17425. [CrossRef] [PubMed]
27. Brouwer, A.M. Standards for photoluminescence quantum yield measurements in solution (IUPAC Technical Report). *Pure Appl. Chem.* **2011**, *83*, 2213–2228. [CrossRef]
28. Würth, C.; Grabolle, M.; Pauli, J.; Spieles, M.; Resch-Genger, U. Relative and absolute determination of fluorescence quantum yields of transparent samples. *Nat. Protoc.* **2013**, *8*, 1535–1550. [CrossRef] [PubMed]
29. Coles, S.J.; Gale, P.A. Changing and challenging times for service crystallography. *Chem. Sci.* **2012**, *3*, 683–689. [CrossRef]
30. Dolomanov, O.V.; Bourhis, L.J.; Gildea, R.J.; Howard, J.A.K.; Puschmann, H. *OLEX2*: A complete structure solution, refinement and analysis program. *J. Appl. Crystallogr.* **2009**, *42*, 339–341. [CrossRef]
31. Sheldrick, G.M. Crystal structure refinement with *SHELXL*. *Acta Crystallogr. Sect. C Struct. Chem.* **2015**, *71*, 3–8. [CrossRef] [PubMed]
32. Sheldrick, G.M. *SHELXT*—Integrated space-group and crystal-structure determination. *Acta Crystallogr. Sect. A Found. Crystallogr.* **2015**, *71*, 3–8. [CrossRef] [PubMed]
33. Campos, E.; Moura, T.F.; Oliva, A.; Leandro, P.; Soveral, G. Lack of Aquaporin 3 in bovine erythrocyte membranes correlates with low glycerol permeation. *Biochem. Biophys. Res. Commun.* **2011**, *408*, 477–481. [CrossRef] [PubMed]
34. Schindelin, J.; Arganda-Carreras, I.; Frise, E.; Kaynig, V.; Longair, M.; Pietzsch, T.; Preibisch, S.; Rueden, C.; Saalfeld, S.; Schmid, B.; et al. Fiji: An open-source platform for biological-image analysis. *Nat. Methods* **2012**, *9*, 676–682. [CrossRef] [PubMed]